INTERNATIONAL JOURNAL FOR NUMERICAL METHODS IN FLUIDS, VOL. 25, 1241–1261 (1997)

AN IMPLICIT MIXED FINITE-VOLUME–FINITE-ELEMENT METHOD FOR SOLVING 3D TURBULENT COMPRESSIBLE FLOWS

L. HALLO, C. LE RIBAULT* AND M. BUFFAT

Ecole Centrale de Lyon/Université Claude Bernard–Lyon 1, Laboratorie de Mécanique des Fluides et d'Acoustique,
URA CNRS 263, 36 Avenue Guy de Collongue, BP 163, F-69131 Ecully Cedex, France

SUMMARY

The development of new aeronautic projects require accurate and efficient simulations of compressible flows in complex geometries. It is well known that most flows of interest are at least locally turbulent and that the modelling of this turbulence is critical for the reliability of the computations. A turbulence closure model which is both cheap and reasonably accurate is an essential part of a compressible code. An implicit algorithm to solve the 2D and 3D compressible Navier–Stokes equations on unstructured triangular/tetrahedral grids has been extended to turbulent flows. This numerical scheme is based on second-order finite element–finite volume discretization: the diffusive and source terms of the Navier–Stokes equations are computed using a finite element method, while the other terms are computed with a finite volume method. Finite volume cells are built around each node by means of the medians. The convective fluxes are evaluated with the approximate Riemann solver of Roe coupled with the van Albada limiter. The standard k–ε model has been introduced to take into account turbulence. Implicit integration schemes with efficient numerical methods (CGS, GMRES and various preconditioning techniques) have also been implemented. Our interest is to present the whole method and to demonstrate its limitations on some well-known test cases in three-dimensional geometries. © 1997 John Wiley & Sons, Ltd.

Int. J. Numer. Meth. Fluids, **25**: 1241–1261 (1997)

No. of Figures: 18. No. of Tables: 0. No. of References: 32.

KEY WORDS: finite volume; upwind scheme; MUSCL; unstructured; 3D; transonic; turbulent

1. INTRODUCTION

The development of new aeronautic projects requires physical investigations of compressible turbulent flows. With problems related to aerodynamic measurement in high-speed flows, the numerical study of these flows is easier than experimental investigations. The problem is then to select efficient and robust numerical methods with suitable turbulence models to simulate these flows. Various researchers have been performed to compare the numerous high-order schemes for the Euler equations available to date.[1,2] The converging point of view is that a finite volume formulation coupled with an upwind conservative scheme is one of the best solutions available. The diffusive part

---

* Correspondence to: C. Le Ribault, Ecole Centrale de Lyon, Laboratorie de Mécanique des Fluides et d'Acoustique, URA CNRS 263, 36 Avenue Guy de Collongue, BP 163, F-69131 Ecully Cedex, France.

CCC 0271–2091/97/111241–21 $17.50

Received November 1994
Revised January 1997

of the Navier–Stokes equations can be evaluated with a classical centred formulation. Furthermore, owing to the ease with which complex geometries can be handled and the possibility of enhancing the solution accuracy through local mesh refinements, unstructured meshes are often employed. A finite element method can be chosen for the discretization of the diffusive part of the Navier–Stokes equations because of its ability to evaluate gradients even on irregular discretization cells.

The mixed finite element–finite volume method, initially developed by Dervieux and coworkers[3–5] for simulation of Euler flows, offers the possibility of using finite volume–finite element coupling on unstructured meshes. The success of this method in solving compressible viscous flows[6] encourages us to extend it to turbulent flows in 2D[7,8] and 3D. The resulting numerical method uses a second-order MUSCL finite volume method for the discretization of the convective fluxes and a second-order finite element method well suited to the evaluation of viscous gradients. It must be pointed out that the convective fluxes are evaluated with the approximate Riemann solver of Roe[9] to ensure good capturing of the discontinuities even in the strongly viscous regions. To model the turbulence, the one-point k–ε closure model, initially developed by Launder and Spalding[10] for incompressible flows, has been introduced. A non-coupled approach has been chosen, following the implementations of Le Ribault,[7] which uses a 2D explicit time integration technique for both the Reynolds-averaged Navier–Stokes equations and the k–ε equations. Wall functions have been introduced to avoid the use of excessive points in the vicinity of walls. The transport equations of the scales of turbulence are only weakly coupled with the aerodynamic vector by introducing the contribution of the kinetic energy of the turbulence in the total energy and by upwinding the convective fluxes of k and ε according to the mass flux of the mean Navier–Stokes equations.

As we are interested in the simulation of steady flows, a linearized implicit time integration scheme and a local time step are employed to compute the solution.

In this paper we first present the Navier–Stokes equations and the introduction of the k–ε model. The mixed finite volume–finite element formulation in two and three dimensions and the implicit time integration technique are then described. Our main goal is to test the whole implicit method and to show that this non-coupled approach is a solid basis for introducing more sophisticated turbulence models, multiple species and combustion. That is our final aim.[11,12]

The whole numerical method has been validated on well-known test cases: an incompressible turbulent jet, a supersonic mixing layer and a three-dimensional pipe.

2. GOVERNING EQUATIONS AND TURBULENCE MODEL

2.1. Mean Navier–Stokes equations

The motion of a viscous gas is governed by the Navier–Stokes equations, which express the conservation of mass, momentum and energy. The governing equations of the mean flow are obtained by an averaging of the Navier–Stokes equations—a Reynolds average is used for the density and the total energy and a Favre average is used for the velocity:

$$\begin{aligned}
&\frac{\partial\bar{\rho}}{\partial t}+\operatorname{div}(\bar{\rho}\tilde{u})=0,\\
&\frac{\partial\bar{\rho}\tilde{u}}{\partial t}+\operatorname{div}(\bar{\rho}\tilde{u}\tilde{u}+\bar{p}I)=-\operatorname{div}(\bar{\rho}\widetilde{u_i''u_j''})+\mu\operatorname{div}(\operatorname{grad}\tilde{u}+\operatorname{grad}^{\mathrm{T}}\tilde{u})-\tfrac{2}{3}\mu\operatorname{grad}(\operatorname{div}\tilde{u}),\\
&\frac{\partial\bar{E}}{\partial t}+\operatorname{div}(\bar{E}\tilde{u})+\operatorname{div}(\overline{E'u''})+\operatorname{div}(\bar{p}\tilde{u})+\operatorname{div}(\overline{p'u''})=\operatorname{div}(\overline{\tau u})+\frac{\gamma\mu}{Pr}\operatorname{div}(\operatorname{grad}\tilde{e}),
\end{aligned}\tag{1}$$

where $\bar{\rho}$ is the density, $\bar{E}$ is the total energy per unit volume, $\tilde{u}_i$ are the velocity vector components along the Cartesian co-ordinates, $\bar{p}$ is the static pressure, τ is the viscous stress tensor, Pr is the

Prandtl number and t is the time. For further developments the mean internal energy $\tilde{e}$ and the mean specific enthalpy $\bar{H}$ are also defined.

To solve the closure problem introduced by the averaging procedure, the Reynolds stress $\widetilde{u_i''u_j''}$ and the turbulent heat fluxes are modelled using a Boussinesq hypothesis:

$$-\bar{\rho}\widetilde{u_i''u_j''} = \mu_{\mathrm{t}}\left(\frac{\partial\tilde{u}_i}{\partial x_j} + \frac{\partial\tilde{u}_j}{\partial x_i} - \frac{2}{3}\frac{\partial\tilde{u}_k}{\partial x_k}\delta_{ij}\right) - \tfrac{2}{3}\bar{\rho}k\delta_{ij}. \tag{2}$$

The other terms introduced by the averaging procedure are $\overline{E'u_i''}$, $\overline{p'u''}$ and $\overline{\tau u}$. For further modelling of these correlations a turbulent thermal conductivity k_{t} is introduced so that

$$\overline{\rho E'u_i''} + \overline{\tau u} = -k_{\mathrm{t}}\frac{\partial\tilde{T}}{\partial x_j} + \tilde{u}_i(\bar{\tau} - \overline{\rho u_i''u_j''}). \tag{3}$$

The turbulent viscosity μ_{t}, is written as a function of two local turbulent scales: the turbulent kinetic energy $k = \frac{1}{2}u_i''u_i''$ and its dissipation rate $\rho\varepsilon = \tau_{ij}\partial u_i''/\partial x_j$. It is defined by $\mu_{\mathrm{t}} = C_\mu\rho k^2/\varepsilon$, where $C_\mu = 0{\cdot}09$.

By multiplying the evolution equations of momentum by the velocity fluctuations and by averaging the resulting equation, one can obtain the governing transport equation for the turbulent kinetic energy $\tilde{k}$:

$$\frac{\partial\bar{\rho}\tilde{k}}{\partial t} + \frac{\partial\bar{\rho}\tilde{k}\tilde{u}_j}{\partial x_j} = \frac{\partial}{\partial x_j}\left[\left(\mu + \frac{\mu_{\mathrm{t}}}{\sigma_k}\right)\frac{\partial\tilde{k}}{\partial x_j}\right] + P_k - \bar{\rho}\tilde{\varepsilon}, \tag{4}$$

where the production of turbulent kinetic energy, P_k, is defined as

$$P_k = -\bar{\rho}\widetilde{u_i''u_j''}\frac{\partial\tilde{u}_i}{\partial x_j}. \tag{5}$$

A second equation is required to evaluate the dissipation rate of the kinetic energy $\tilde{\varepsilon}$. After introducing assumptions about production and dissipation, the corresponding transport equation can be written as

$$\frac{\partial\bar{\rho}\tilde{\varepsilon}}{\partial t} + \frac{\bar{\rho}\tilde{\varepsilon}\tilde{u}_j}{\partial x_j} = \frac{\partial}{\partial x_j}\left[\left(\mu + \frac{\mu_{\mathrm{t}}}{\sigma_\varepsilon}\right)\frac{\partial\tilde{\varepsilon}}{\partial x_j}\right] + C_{\varepsilon 1}P_k\frac{\tilde{\varepsilon}}{\tilde{k}} - C_{\varepsilon 2}\bar{\rho}\frac{\tilde{\varepsilon}^2}{\partial\tilde{k}}. \tag{6}$$

All the quantities are made dimensionless using three characteristic scales, ρ_0, u_0 and l_0, so that the modelled Navier–Stokes equations can be written in the vectorial form

$$\underbrace{\frac{\partial q}{\partial t}}_{\text{temporal derivative}} + \underbrace{\operatorname{div} F(q)}_{\text{convective fluxes}} = \underbrace{\frac{1}{Re}\operatorname{div} R(q)}_{\text{viscous terms}} + \underbrace{\omega(q)}_{\text{source terms,}} \tag{7}$$

where

$$q=\begin{bmatrix}\bar\rho\\ \bar\rho\vec{\tilde u}\\ \bar E\\ \bar\rho\tilde k\\ \bar\rho\tilde\varepsilon\end{bmatrix},\qquad F(q)=\begin{bmatrix}\bar\rho\vec{\tilde u}\\ \bar\rho\vec{\tilde u}\otimes\vec{\tilde u}(\bar p+\frac{2}{3}\bar\rho\tilde k)\vec{\vec{I}}\\ (\bar E+\bar p+\frac{2}{3}\bar\rho\tilde k)\vec{\tilde u}\\ \bar\rho\vec{\tilde u}\tilde k\\ \bar\rho\vec{\tilde u}\tilde\varepsilon\end{bmatrix},$$

$$R(q)=\begin{bmatrix}0\\ \vec{\vec{\sigma}}\\ \vec{\vec{\sigma}}\vec{\tilde u}-\left(\dfrac{\gamma\mu}{Pr}+\dfrac{\gamma\mu_{\mathrm{t}}}{Pr_{\mathrm{t}}}\right)\operatorname{grad}\tilde e-\dfrac{\mu_{\mathrm{t}}}{\sigma_k}\operatorname{grad}\tilde k\\ \left(\mu+\dfrac{\mu_{\mathrm{t}}}{\sigma_k}\right)\operatorname{grad}\tilde k\\ \left(\mu+\dfrac{\mu_{\mathrm{t}}}{\sigma_\varepsilon}\right)\operatorname{grad}\tilde\varepsilon\end{bmatrix}.$$

The source term $\omega(q)$ is defined as

$$\omega(q)=\begin{bmatrix}P_k-\bar\rho\tilde\varepsilon\\ C_{\varepsilon 1}\dfrac{\tilde\varepsilon}{\tilde k}P_k-C_{\varepsilon 2}\bar\rho\dfrac{\tilde\varepsilon^2}{\tilde k}\end{bmatrix}.$$

The values of the constants are the classical values obtained in the incompressible case: $\sigma_k=1, \sigma_\varepsilon=1{\cdot}3$, $C_{\varepsilon 1}=1{\cdot}44$, $C_{\varepsilon 2}=1{\cdot}92$.

This system is closed after one has chosen the average state equation. The perfect gas law is used, written as

$$\bar p=(\gamma-1)[\bar E-\tfrac{1}{2}\bar\rho(\tilde u_1^2+\tilde u_2^2+\tilde u_3^2)-\bar\rho\tilde k]. \tag{8}$$

To preserve the perfect state relation between $\bar p$ and the mean total energy $\bar E$, an appropriate change of variables has been defined by setting $\bar p'=\bar p+\frac{2}{3}\bar\rho\tilde k$. Consequently we get

$$\bar p'=(\gamma-1)[\bar E-\tfrac{1}{2}\bar\rho(\tilde u_1^2+\tilde u_2^2+\tilde u_3^2)+\beta\bar\rho\tilde k], \tag{9}$$

where $\beta=-1+2/3(\gamma-1)$. Choosing $\bar E'=\bar E+\beta\bar\rho\tilde k$, the relation between $\bar p'$ and $\bar E'$ has the classical form

$$\bar p'=(\gamma-1)[\bar E'-\tfrac{1}{2}\bar\rho(\tilde u_1^2+\tilde u_2^2+\tilde u_3^2)]. \tag{10}$$

This change of variable has the interesting consequence that a standard Riemann solver can be used to approximate the hyperbolic part of the averaged Navier–Stokes equations. The equation of evolution of energy has only to be replaced by the equation of evolution of $\bar E'$, which is the classical evolution equation for $\bar E$ plus some additional terms from the evolution equation of $\beta\bar\rho\tilde k$.

The above equations describe the three-dimensional motion of a compressible turbulent flow. The standard k–ε model allows the computation of most test cases, but some limitations exist because compression and compressibility effects on the turbulence are not fully taken into account in the model.

2.2. *Wall functions*

The derivation of the k–ε model is made under the hypothesis of high-Reynolds-number flows. The first possibility is to use a low-Reynolds-number model, but such models require a considerable number of nodes in the vicinity of the wall. Wall functions[13] have then been preferred to model the near-wall region. The equations for the mean flow and turbulence scales are solved up to a distance δ away from the wall and the wall functions are used as boundary conditions at the boundary wall. The dimensionless wall distance y^+ and the friction velocity u_f are introduced such that $y^+ = \rho u_\mathrm{f} y/\mu$ and $u_\mathrm{f} = \sqrt{(\tau_\mathrm{p}/\rho)}$, where τ_p is the parietal tension. The wall functions can be written as

$$\tilde{u} \cdot \tilde{t} = \begin{cases} u_\mathrm{f} y^+ & \text{if } y^+ < 11{\cdot}6, \\ u_\mathrm{f}[(1/K)\log\, y^+ + C] & \text{if } y^+ \geqslant 11{\cdot}6, \end{cases}$$

where $\tilde{u} \cdot \vec{t}$ is the tangential velocity. K and C are the Von Karman universal constants, respectively equal to 0·419 and 5·445. For the turbulence quantities, equilibrium between production and dissipation rates gives the proper boundary conditions $\tilde{k} = u_\mathrm{f}^2/\sqrt{C_\mu}$ and $\tilde{\varepsilon} = u_\mathrm{f}^3/\delta K$.

These laws have been established for incompressible flows, but experiments with compressible boundary layers show that they remain valid in the absence of strong density variations.

3. MIXED FINITE-VOLUME–FINITE-ELEMENT METHOD

The numerical method is an extension of the mixed finite volume-finite element method initially developed to solve the unsteady Navier–Stokes equations.[6] The approach presented below operates an unstructured finite element mesh, using a MUSCL upwind formulation for the hyperbolic terms and a Galerkin finite element method for the diffusive part of the Navier–Stokes equations. Here the general framework of the mixed finite element–finite volume method to solve (7) will be presented. In Section 3.1 we will outline the dual finite element–finite volume mesh and in Section 3.2 the spatial discretization of the averaged equations. The time discretization and the boundary conditions are then discussed in Sections 3.3 and 3.4 respectively.

3.1. *Dual finite volume mesh*

We assume that Σ is a polygonal bounded domain of $\mathbb{R}^2$ ($\mathbb{R}^3$). Let T_h be a standard triangulation (tetrahedrization) of Σ. Starting from T_h, a dual finite volume mesh is built such that there exists a bijective operator from the finite element mesh to the finite volume mesh and such that the finite volume mesh covers exactly the domain Σ.

The following notation is also introduced:

(a) *meas* C_i—the control area (volume) of the finite volume cell C_i
(b) N_i—the number of neighbouring vertices of i.

In the two-dimensional case the finite volume cell C_i associated with the vertex i is defined as follows.

1. Every triangle of T_h having node i as a vertex is subdivided by means of its medians.
2. The cell C_i is then defined as the union of the resulting subtriangles having node i as a vertex; see Figure 1.

This concept of two-dimensional construction is extendible to the three-dimensional case. A dual finite volume partition is derived from the construction of median planes. For each vertex i a finite volume cell is defined. Every tetrahedron having i as a vertex is subdivided into subtrahedra by means

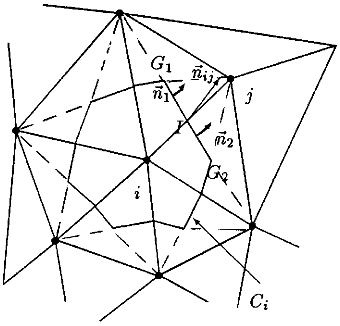

Figure 1. Control area C_i in 2D

of planes containing an edge and the middle of the opposite edge. Then the cell C_i is the union of the subtrahedra having i as a vertex; see Figure 2.

3.2. *Spatial discretization of mean flow*

Starting from the general variational formulation of the averaged Navier–Stokes equations (7), a discrete formulation is obtained by using the characteristic function φ_i of the finite volume cell C_i as the test function for the convective part of the equation and the usual piecewise linear finite element basis function ϕ_i as the test function for the diffusion and source terms:

$$\int_{C_i}\left(\frac{\partial q}{\partial t} + \mathrm{div}\, F(q)\right)\varphi_i\,\mathrm{d}v = \int_{\sum_{C_i}^{T}} [\mathrm{grad}\, R(q) + \omega(q)]\phi_i\,\mathrm{d}v. \tag{11}$$

Green's theorem is applied to the convective fluxes, while the viscous terms are integrated by parts. The temporal derivative is integrated in a straightforward way by considering that q_i is constant over

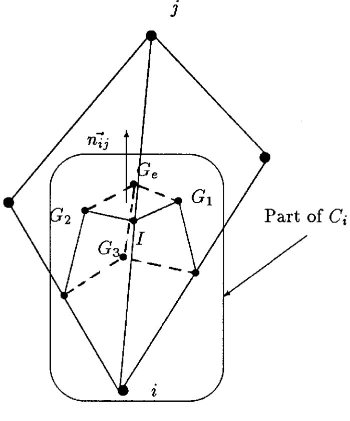

Figure 2. Part of control volume C_i in 3D

the cells, which is fully equivalent to using a finite element discretization with a mass-lumping approximation. After these manipulations the variational formulation is written as

$$\frac{\partial}{\partial t}\int_{C_i} q\,\mathrm{d}v + \oint_{\partial C_i} F(q, \vec{n}_i)\,\mathrm{d}\sigma = -\int_{\sum_{C_i}^{T}} [R(q)\cdot \operatorname{grad}\phi_i + \omega(q)\phi_i]\,\mathrm{d}v + \oint_{\Gamma} R(q, \vec{v})\phi_i\,\mathrm{d}\sigma,$$

where $\vec{n}_i$ is the outward unit vector to ∂C_i, such that $\vec{n}_i = (n_{ix}, n_{iy}, n_{iz})$ in three dimensions, and $\vec{v}$ is the outward unit vector to the boundary Γ.

The discretization of the viscous, convective and source terms will now be defined.

Viscous terms

Since the viscous part of the compressible Navier–Stokes equations is parabolic, no oscillations can arise in the diffusion-dominated region, so the discretization is carried out in a centred way with a standard second-order finite element formulation. Bear in mind that with each vertex i is associated the test function ϕ_i lying in a space of continuous, linear in each element, functions and which fulfils $\phi_i(j) = \delta_{ij}$. Thus any function f and its gradient are interpolated over a finite element T by

$$f(x, y, z)|_T = \sum_{j\in T} f(j)\phi_j|_T(x, y, z), \qquad \operatorname{grad} f(x, y, z)|_T = \sum_{j\in T} f(j)\operatorname{grad}\phi_j|_T(x, y, z) = \text{constant}.$$

This technique is applied directly to the diffusive flux vector $R(q)$. The details of this manipulation can be found in the work of Rostand.[6]

The integral $\oint_\Gamma R(q, \vec{v})\phi_i\,\mathrm{d}\sigma$ is neglected.

Convective terms

The scheme will be completely defined once the approximation of the convective terms has been made precise. Upwinding is introduced in the computation of the convective terms through the numerical flux function Φ of a first-order-accurate upwind scheme by

$$\oint_{\partial C_i} F(q, \vec{n}_i)\,\mathrm{d}\sigma = \sum_{k=1}^{N_i} \Phi(q_i, q_k, \vec{n}_{ik}). \tag{12}$$

The numerical flux function used is the approximate Riemann solver (ARS) of Roe[9] with the entropy correction of Harten and Hyman:[14]

$$\Phi(q_-, q_+, \vec{n}_i) = \tfrac{1}{2}[F(q_-, \vec{n}_i) + F(q_+, \vec{n}_i)] - \tfrac{1}{2}|A(\tilde{q}, \vec{n}_i)|(q_+ - q_-),$$

where

$$\tilde{\rho} = \surd(\rho_-\rho_+), \qquad \tilde{q} = \frac{q_+O + q_-}{O+1}, \qquad O = \sqrt{\left(\frac{q_+}{q_-}\right)}, \qquad \tilde{q} = \begin{cases}\vec{v}\\ H\end{cases}$$

and

$$A = \frac{\partial F}{\partial q} = R\Lambda R^{-1}, \qquad |A| = R|\Lambda|R^{-1}.$$

It is evaluated in a standard way, between vertices i and k, as a projection of the approximate flux on the direction normal to the boundary of the cell. In order to prevent any of the eigenvalues λ_i from vanishing, one approximates $|\lambda|$ through $Q(\lambda)$:[14]

$$|\lambda| = Q(\lambda) = \operatorname{diag}\begin{cases}\frac{1}{2}(\lambda_2/\delta = \delta), & |\lambda| < \delta,\\ |\lambda|, & |\lambda| \geqslant \delta,\end{cases}$$

where δ is a small parameter.

The normal vector is obtained through the formulation

$$\vec{n}_{ik} = \oint_{\partial S_{ik}} \vec{n}_i \, \mathrm{d}\sigma.$$

In two dimensions there are two contributions $\vec{n}_1$ and $\vec{n}_2$ from the two segments $[G_1; I]$ and $[I; G_2]$ constructed from the barycentres of adjacent elements (see Figure 3 on the left). In three dimensions the segments become surfaces and there are many contributions from adjacent tetrahedra (see Figure 3 on the right).

The numerical integration described previously leads to approximations which are only first-order-accurate in space. A second-order MUSCL-like extension is used[15] to improve the precision of the method without changing the approximation space. The spatial precision of the flux is increased by interpolating the arguments of the numerical flux in equation (12) at the boundaries of the cell ∂C_i (internodal values between nodes i and k):

$$q_- = q_i + \tfrac{1}{2}\,\mathrm{grad}\; q_i \cdot \vec{n}_{ik}, \qquad q_+ = q_k - \tfrac{1}{2}\,\mathrm{grad}\; q_k \cdot \vec{n}_{ik}.$$

From a solution that is constant within a cell, a piecewise linear solution is calculated over the cell. This is an extension of the MUSCL method[15] to the finite element method,[16,17] because the gradients of the state vector q are computed with the finite element technique:

$$\mathrm{grad}\; q_i = \frac{\int_{C_i} \mathrm{grad}\; q\phi \,\mathrm{d}v}{\int_{C_i} \mathrm{d}v} = \frac{1}{meas\; C_i} \sum_{\Sigma_{C_i} T} \frac{meas\; T}{dim} \sum_{j=1}^{dim} q_i^j \,\mathrm{grad}\; \phi_i|_T,$$

where dim is the number of nodes of finite elements, three in 2D and four in 3D, $meas\; C_i$ is the control area in 2D, or control volume in 3D, of the finite volume cell C_i and $meas\; T$ is the control area in 2D, or control volume in 3D, of the finite element T.

A limiter technique is finally applied to damp off numerical oscillations. The scheme of $O(\Delta x^2)$ is preserved in areas where the gradient of q is smooth, while in the vicinity of discontinuities, i.e. shocks, the scheme becomes increasingly first-order upwind, which introduces numerical dissipation with a beneficial dampening effect. Thus a quasi-TVD scheme is obtained.[18] Using a one-dimensional limiter, the arguments in the numerical flux become

$$q_- = q_i + \tfrac{1}{2}\,\lim(2\;\mathrm{grad}\; q_i \cdot \vec{n}_{ik} - (q_k - q_i), (q_k - q_i)),$$
$$q_+ = q_k - \tfrac{1}{2}\lim(2\;\mathrm{grad}\; q_k \cdot \vec{n}_{ik} - (q_k - q_i), (q_k - q_i)),$$

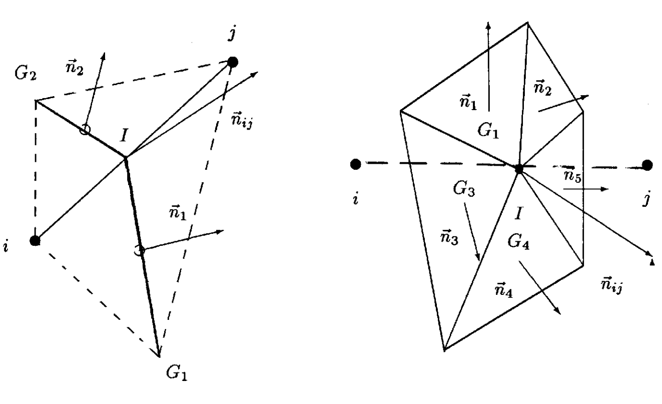

Figure 3. Construction of $\vec{n}_{ij}$: 2D on left; 3D on right.

where a combination of the van Leer limiter and the van Albada limiter[19] is utilized in accordance with the work of Sacquepee:[20]

$$\lim(a,b)=\begin{cases}\dfrac{(a^2+\varepsilon)b+(b^2+\varepsilon)a}{a^2+b^2+2\varepsilon}, & ab>0,\\ 0, & ab\leqslant 0.\end{cases}$$

Source terms

The source terms are written in the generic form

$$\int_{\Sigma_{C_iT}} \omega\phi_i\,\mathrm{d}v.$$

The integration is obtained through the classical finite element manipulations:

$$\begin{aligned}\int_{\Sigma_{C_iT}} \omega\phi_i\,\mathrm{d}v &= \sum_{j=1}^{N_i}\int_{T_j}\omega\phi_i\,\mathrm{d}v\\ &= \sum_{j=1}^{N_i}\int_{T_j}\sum_{k=1}^{dim}\omega_k\phi_k\phi_i\,\mathrm{d}v\\ &= \sum_{j=1}^{N_i}\sum_{k=1}^{dim}\omega_k\int_{T_j}\phi_k\phi_i\,\mathrm{d}v\\ &= \sum_{j=1}^{N_i} meas\ T_j\sum_{k=1}^{dim}\omega_k.\end{aligned}$$

*Coupling with extra equations; k–*ε model

The coupling between the average Navier–Stokes equations and the transport equations of the turbulent scales k and ε is weakly achieved by means of the change of variable between the total energy and the total energy including the turbulent kinetic energy (see Section 2.1). This change of variable has the beneficial effect of improving the precision of the solution, but it does not prevent numerical oscillations in the advection-dominated regions. A solution proposed by Larrouturou[21] is to upwind the convective terms of the extra equations in accordance with the mean mass flux splitting from the averaged Navier–Stokes equations.

3.3. Time discretization

The spatial discretization procedures described in the previous subsections lead to a semidiscretized formulation which has to be integrated to reach steady state. An explicit version can be derived by using a diagonal mass-lumped matrix, which effectively amounts to assuming a constant value of q over the cell C_i equal to q_i.

This is the explicit forward Euler scheme. The time step Δt_i can be set equal to a constant for first-order-accurate time integration or taken equal to the value matching a local CFL stability condition for steady state computation:

$$\int_{C_i}\left(\frac{\partial q}{\partial t}\right)\mathrm{d}v = meas\ C_i\frac{q_i^{n+1}-q_i^n}{\Delta t_i}+(K(q^n))_i, \tag{13}$$

where $(K(q^n))_i$ denotes the sum of the fluxes (convective, viscous, source terms) evaluated at time level n.

This explicit scheme is easy to implement and can be solved without any matrix inversion. For the Euler equations the stability condition leads to the quantity

$$C_1 = (|u| + c)\frac{\Delta t}{\Delta x}.$$

For the Navier–Stokes equations the stability condition leads to the quantity

$$C_2 = \frac{1}{\rho\, Re\, Pr}\frac{\Delta t}{\Delta x_2},$$

which must of magnitude one for the explicit scheme. This means that the time step is bounded by a value proportional to the square of the minimum cell height.

In order to remove this restrictive condition, one attempts to design implicit algorithms. For that purpose a linearized Newton procedure for each term is applied to equation (13) after we have replaced q^n by q^{n+1}.

A Taylor series expansion gives

$$(K(q^{n+1}))_i = (K(q^n))_i + \frac{\partial (K(q^n))_i}{\partial t} + O(\Delta t^2),$$

with

$$\frac{\partial (K(q^n))_i}{\partial t} = \frac{\partial (K(q^n))_i}{\partial q}\frac{\partial q}{\partial t}\bigg|^n$$

and

$$q^{n+1} = q^n + \frac{\partial q}{\partial t}\bigg|^n \Delta t + O(\Delta t^2).$$

The implicit formulation is given by

$$\frac{\partial q}{\partial t}\bigg|^n = \frac{q^{n+1} - q^n}{\Delta t} + O(\Delta t^2),$$

$$(K(q^{n+1}))_i = (K(q^n))_i + \frac{\partial (K(q^n))_i}{\partial q}(q^{n+1} - q^n) + O(\Delta t^2).$$

One obtains the equivalent discrete system

$$\left(\frac{meas\ C_i}{\Delta t} - \frac{\partial (K(q^n))_i}{\partial q}\right)\delta q^n = (K(q^{n+1}))_i, \tag{14}$$

where $\delta q^n = q^{n+1} - q^n$ and $\partial(K(q^n)_i)/\partial q$ is the Jacobian of the fluxes.

The exact linearization of the convective flux $F(q)$ is quite complicated in the general case, so a simpler form of matrix is generally chosen[4].

1. The matrix $\partial(K(q^n))_i/\partial q$ is replaced by one relying on the first-order-accurate approximation.
2. Only the homogeneous part of the Jacobian matrix has been retained.
3. The turbulent contributions are neglected in the linearization of the aerodynamic state vector, in such a way that a decoupled approach can be used.

The linearization of diffusive and source terms is straightforward, by considering constant gradients and mean state vector values per element.

To solve the full set of equations (14) at each time step, the averaged Navier–Stokes equations are first solved with the values of μ_t and $\tilde{k}$ taken from the turbulent variables at time level n, then the two transport equations for $\tilde{k}$ and $\tilde{\varepsilon}$ are solved with the mean aerodynamic values taken at time level n. The coupling is achieved with the change of variable and with the use of the mass flux for upwinding convective fluxes.

3.4. Boundary conditions

Since the state vector q is collocated at the cell vertex, boundary conditions can be either imposed on the boundary nodes or satisfied within the weak formulation through a numerical flux. These two possibilities are used in the numerical method. Dirichlet conditions are imposed on solid walls for k and ε, while the other boundary conditions are imposed through numerical fluxes defined below.

Solid walls

A first estimate of the skin friction velocity u_f is computed from the tangential velocity $\vec{u} \cdot \vec{t}$ using the linear law $u_f = \sqrt{(\vec{u} \cdot \vec{t})/\tilde{\rho}\delta}$. In the two-dimensional case the tangent vector is given by the direction of the mean velocity on the cell boundary. In three dimensions the direction of the tangential velocity is given by the velocity at the internal node of the tetrahedron.

If $y^+ > 11{\cdot}6$, a new evaluation of u_f is computed from the logarithmic law using a Newton method. The viscous stress $\tau_p = \rho u_f^2$, which appears in the variational formulation, is calculated with the one-dimensional finite element theory and imposed on each boundary cell of Γ:

$$\int_{\Gamma_i} \tau_p \phi_i \, dl = \int_{\Gamma_i} \rho u_f^2 \phi_i \, dl. \tag{15}$$

Inlet and outlet boundary sections

The numerical flux of Steger and Warming[22] is evaluated from the boundary nodes and an external flow field as shown in Figure 4 in the two-dimensional case. In the three-dimensional context the boundary cells can be really complicated to represent, but the construction procedure is identical to the one in Figure 3 on the right. This external flow field, referenced as q_∞, uses physical values as well as numerical values obtained from compatibility relations.[23]. These relations provide the numerical values for subsonic inlets (imposed mass flow rate or direction and total conditions) and supersonic and subsonic outlets (static pressure imposed). The supersonic inlet flow field state is not modified. Concerning the implicit treatment, the numerical fluxes applied within the weak formulation are linearized, but the compatibility relations stay explicit. This approach is both robust and accurate for steady calculations because it yields some beneficial fluctuations during convergence.

Slip or symmetry conditions

A centred Euler flux is applied on these boundaries, specifying that the normal velocity is zero. A compatibility relation is used to evaluate the pressure, taking the internal field into account.

3.5. Solution algorithms

This decoupled approach has proved to be stable enough, even for large time steps, with an efficient routine for the resolution of the linear system.

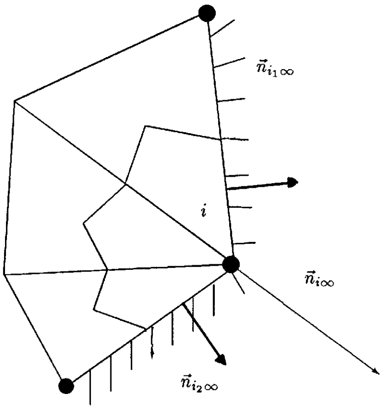

Figure 4. Boundary control area and outward-pointing vector in 2D

The linear system arising from the discretization is $Ax = b$, where A is an asymmetric, sparse, $(dim + 1) \times (dim + 1)$ block matrix of dimension $(dim + 1) \times N$, with N the number of discretization nodes. A compact storage technique is used, into which only the non-zero blocks are stored. For line i of the metric these non-zeros correspond to nodes physically connected to node i by means of the convective flux, diffusive gradient or boundary condition. An evaluation of the number of connected nodes is given by the number of nodes neighbouring i, since the implicit linearization is only first-order in space.

The resolution of equations is the main goal of a previous paper[24] on the testing of various numerical methods for solving linear systems arising from this kind of discretization. As a result of this extensive work, a CGS solver with SSOR preconditioning[25] has been preferred to the methods based on Krylov subspaces.[26,27]

4. VALIDATION TEST CASES

Three typical compressible turbulent flows are simulated: a low-Mach-number two-dimensional axisymmetric turbulent jet, a two-dimensional turbulent supersonic mixing layer and a three-dimensional pipe. Our goal is twofold.

1. First we want to evaluate the spatial accuracy of a 3D calculation compared with a 2D calculation.
2. The second objective is to validate the decoupled approach for 3D flows. This has to be considered as work in progress, so the results presented here are only preliminary results. The boundary conditions include symmetry or slip walls as well as inlet and outlet sections and solid walls.

4.1. Turbulent low-Mach-number jet

This is a 2D axisymmetric annular jet that is weakly heated. It has been studied experimentally by Bahraoui[28] and numerically by Brun.[29] The simulation is carried out from the potential zone of the jet ($x/D = 4\cdot5$) to a section such as $x/D = 12\cdot5$. For the inlet boundary the total pressure, total enthalpy, $\tilde{k}$ and $\tilde{\varepsilon}$ are deduced from experiment. The flow is subsonic with a maximum Mach number equal to 0·08. The outlet pressure is atmospheric pressure. Two computations have been done: a 2D axisymmetric one with 600 nodes and a true 3D calculation. The 3D mesh is obtained from a quarter-rotation of the 2D plane around the x-axis (with five radii) and is shown in Figure 5.

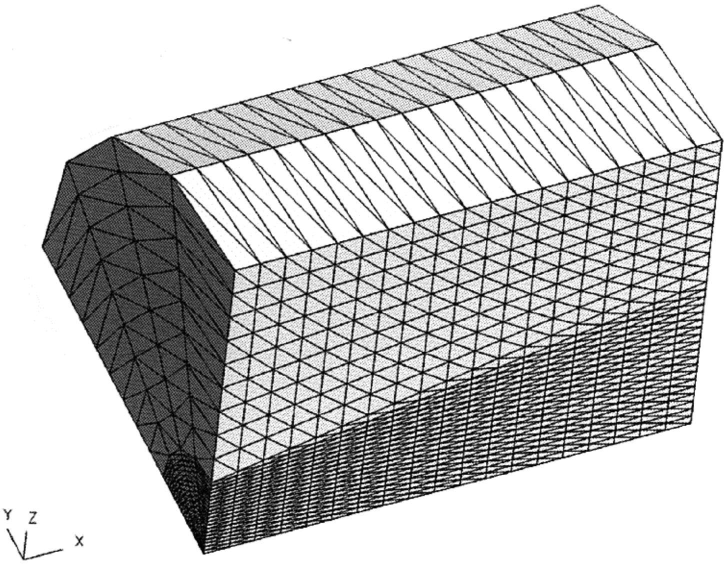

Figure 5. Three-dimensional mesh of turbulent low-Mach-number jet

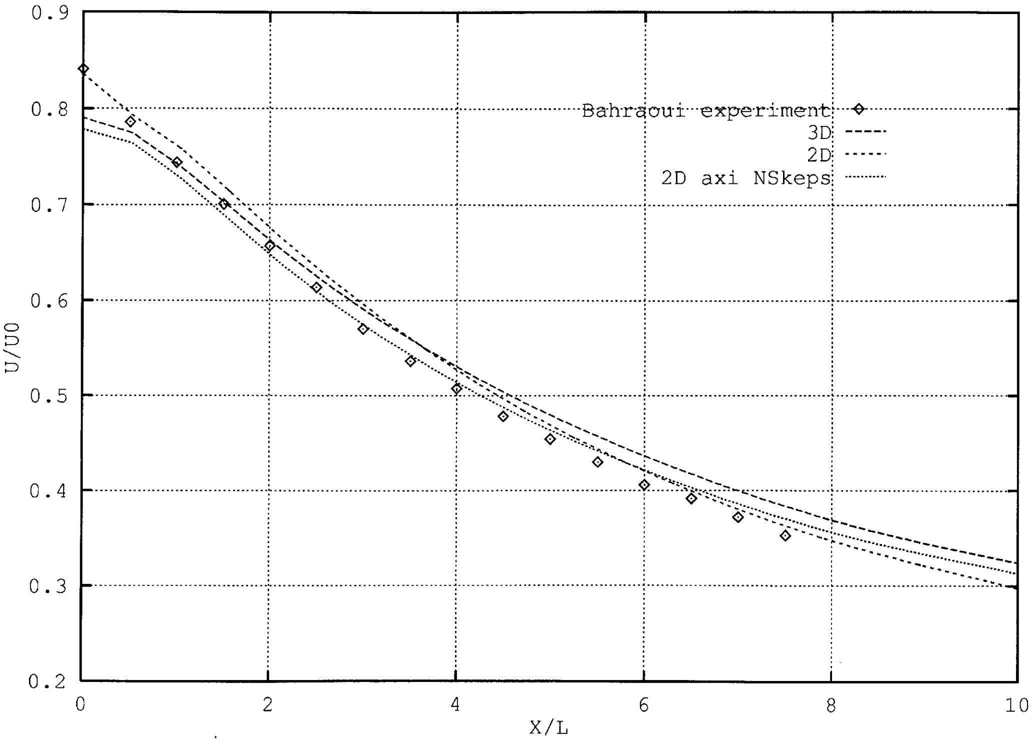

Figure 6. Low-Mach-number jet: axial profile of $\tilde{u}_1$

Three calculations are presented here: two with our numerical method (a 2D axisymmetric one and a full 3D calculation) and a 2D axisymmetric one with the NSkeps numerical method.[7] This numerical method is also based on a mixed finite element–finite volume discretization, but the boundary conditions are different and an explicit time integration scheme is used. Our results are referenced hereafter as 2D and 3D and the NSkeps results are referenced as 2D axi NSkeps. Figure 6 shows the computed velocity component $\tilde{u}_1$ along the axis. The experimental results of Bahraoui are superimposed on the 3D and 2D axisymmetric computational results. Figure 7 shows the radial profile of u_1 at the section $x/D = 8$. Figure 8 shows the decrease in $\tilde{k}$ and $\tilde{\varepsilon}$ along the axis from both 2D axi and 3D Natur calculations.

A small difference exists between the 2D and 3D results. It can probably be attributed to some 3D effect on the size of cells, which increases the numerical diffusion. This was already noticed with eular simulations, where the quality of the mesh (ratio of the element dimensions) was not very good owing to the poor number of nodes used for the rotation of the 2D mesh.

A global view of the resulting flow is shown in Plate 1: the iso-values of Mach number are presented.

4.2. *Supersonic mixing layer*

The computed supersonic mixing layer corresponds to the experiment realized by Goebel *et al.*[30] The Mach numbers of the two incoming fluids are respectively 1·91 and 1·37. The mean freestream velocity ratio U_1/U_2 is 0·58 and the mean density ratio ρ_1/ρ_2 is 1·56.

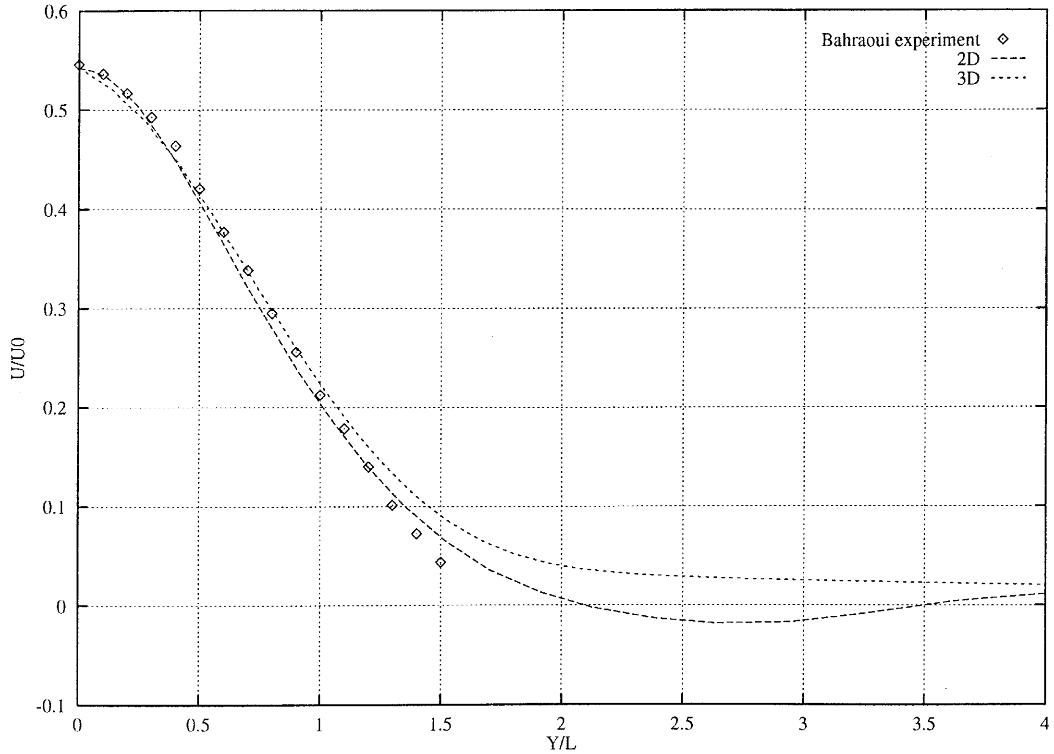

Figure 7. Low-Mach-number jet: radial profile of $\tilde{u}_1$ (at $x/d = 8$)

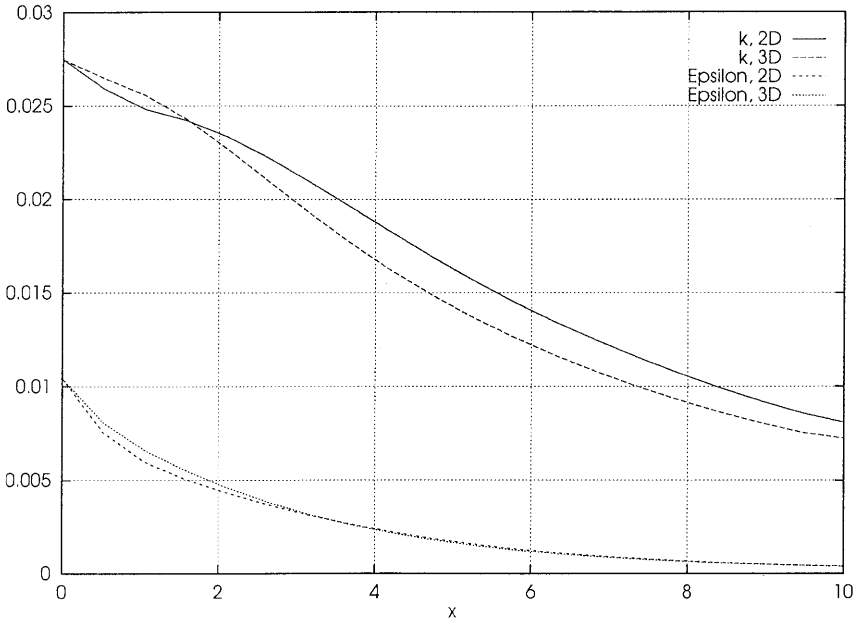

Figure 8. Low-Mach-number jet: decrease in $\tilde{k}$ and $\tilde{\varepsilon}$ along axis

In non-dimensional units of the geometry is one unit high by eight units long. It is shown in Figure 9.

The computation begins in a section where the mixing layer is fully developed ($x = 0$); the outlet section is at $x = 8$. The flow field has similarity properties along the x-axis. Simulations have also been done in the two-dimensional case. To construct the three-dimensional mesh, a translation of three nodes of the two-dimensional mesh has been carried out such that there are three planes in the z-direction.

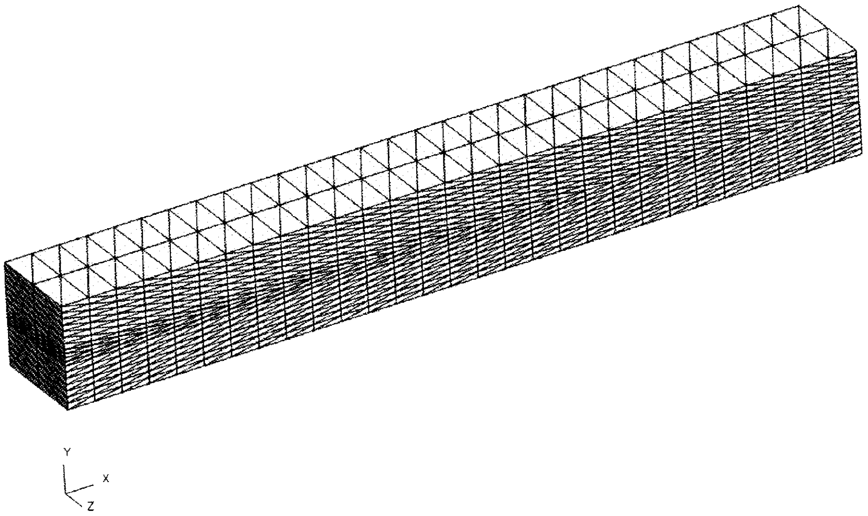

Figure 9. Three-dimensional mesh of supersonic mixing layer

The computed and experimental similarity profiles of the mean velocity $(U - U_2/U_1 - U_2)$ (Figure 10) and the correlation $\widetilde{u''_1 u''_2}/(U_1 - U_2)^2$ (Figure 11) are plotted in three sections in accordance with the thickness of the mixing layer. The velocity profiles exhibit good agreement. The correlation profiles present a peak near the centre of the mixing layer; although its shape is close to the experimental results, its level is different. The same discrepancy occurs in the two-dimensional computation. This can be explained by two facts.

1. There is no experimental information about the level of $\tilde{\varepsilon}$ in the inlet section, so the inflow conditions for $\tilde{\varepsilon}$ have been computed assuming that the turbulent viscosity is 100 times greater than the fluid viscosity, which might not correspond exactly to reality.
2. The second point is that there are no compressibility terms in the standard k–ε model, which are not negligible in the mixing zone.

Two criteria are used to verify that the converged state is obtained: the first is the balance of inlet and outlet mass flows, which must be zero, and the second is the decrease in some norms during time iterations. Two norms are used in our calculations: the first is the maximum correction over the whole mesh, the $L1$ norm, and the second is the $L2$ norm, which is the mean spatial correction. These norms are evaluated only on the density, because a similar behaviour has been noticed for all state vector variables.

The convergence history of the $L1$ and $L2$ norms corresponding to the mixing layer calculation is presented in Figure 12. A lower limit is reached in roughly 300 iterations, with the number CFL increasing as the inverse of the $L2$ residual.

A global view of the resulting flow is shown in Plate 2: the iso-values of turbulent kinetic energy are presented. The two-dimensional feature of the flow as well as the linear growth rate of the mixing layer can be noticed.

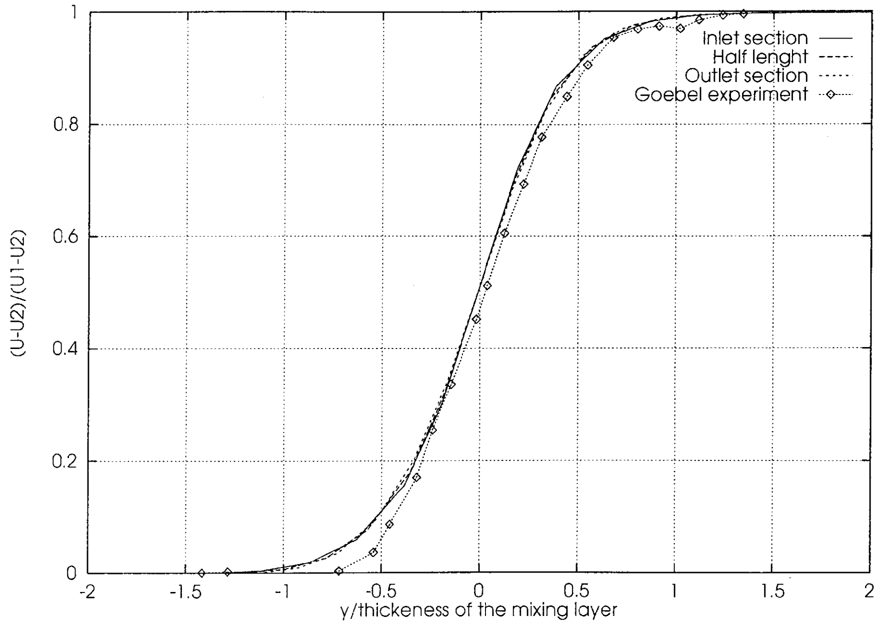

Figure 10. Supersonic mixing layer: dimensionless profiles of $\tilde{u}_1$

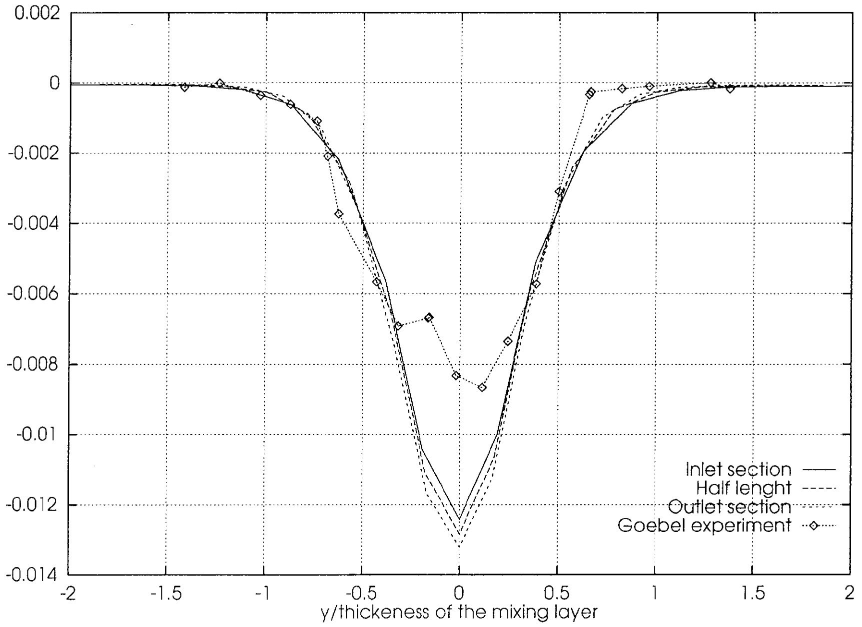

Figure 11. Supersonic mixing layer: dimensionless profiles of u_1'', u_2''

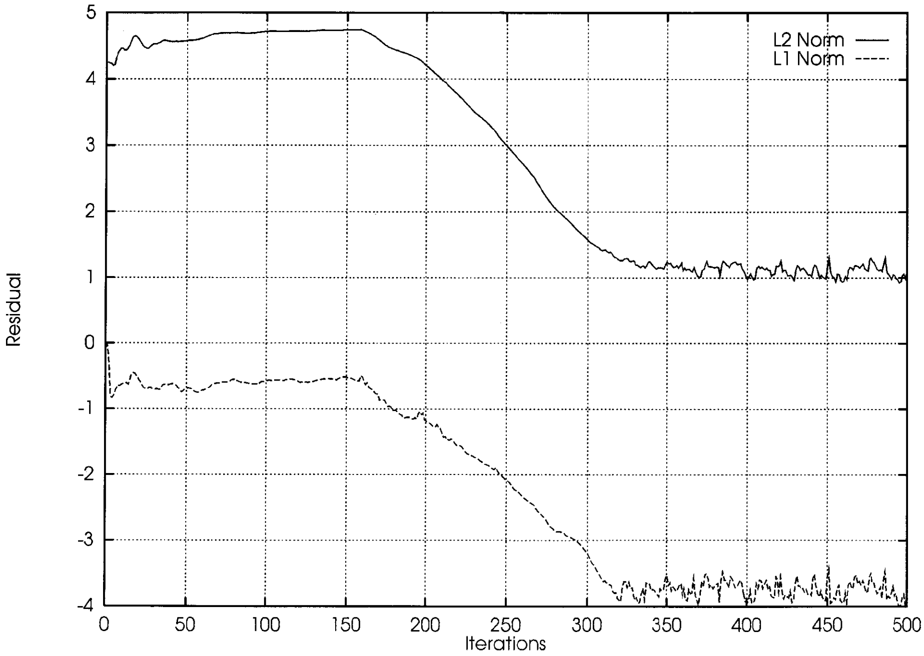

Figure 12. Supersonic mixing layer: convergence history of $L1$ and $L2$ norms

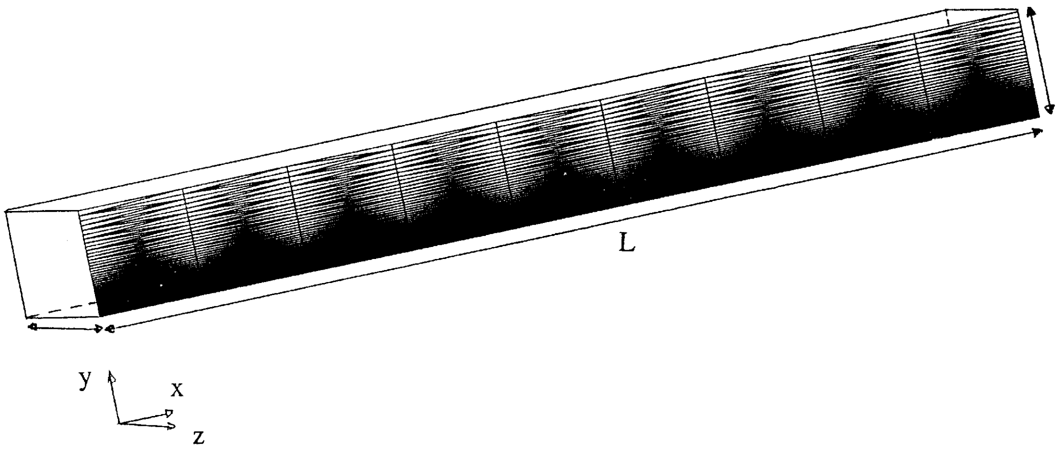

Figure 13. Three-dimensional mesh of pipe

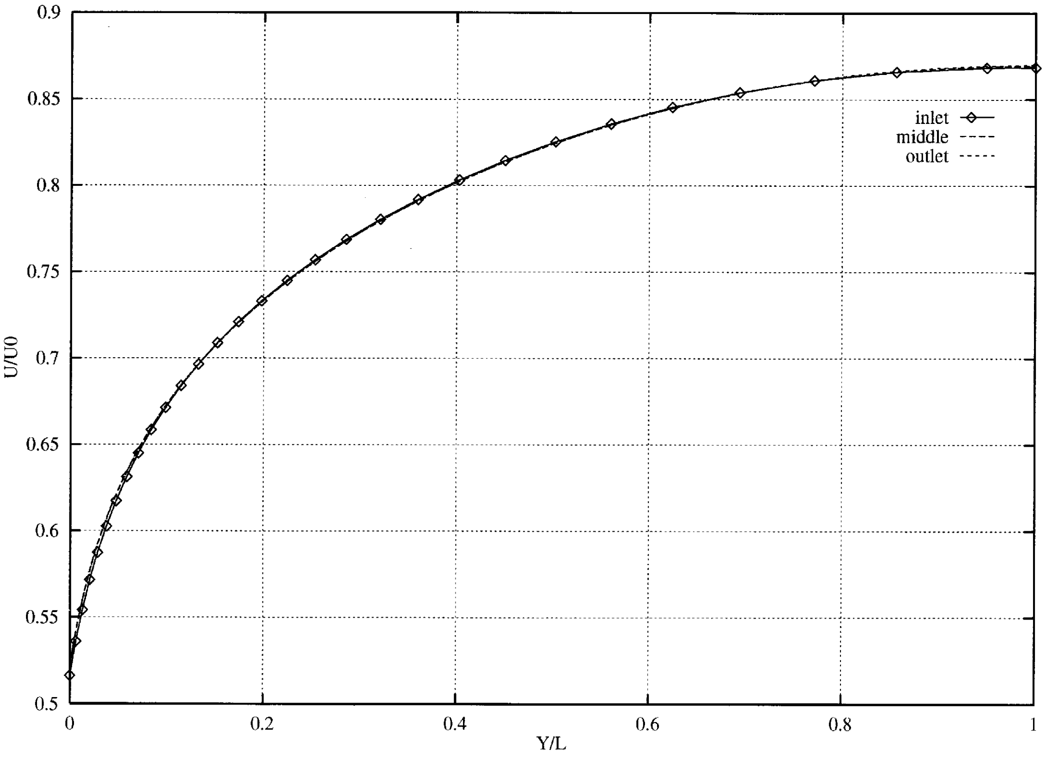

Figure 14. Pipe: profiles of velocity at inlet, middle and outlet sections

4.3. Three-dimensional pipe

In order to validate the turbulent boundary conditions on a solid wall in three dimensions, an incompressible pipe is computed. This case has been chosen for its simplicity and because experimental data are available.[31] The flow is induced by a pressure gradient between the inflow and outflow sections. The turbulence is fully developed and the profiles of velocity and turbulent scales are independent of the section. The distance between the two plates is 0·18 m and the velocity at the middle height of the pipe is 10·5 m s^{-1}. The Reynolds number is 57,000. On the wall the friction velocity is 0·39 m s^{-1}.

The three-dimensional mesh has been obtained from a translation of the two-dimensional mesh (Figure 13). There are 10 nodes in the x-direction, 60 nodes in the y-direction with a geometrical progression near the wall where the gradients are strong, and three nodes in the z-direction. Inlet boundary conditions are provided by a one-dimensional code[32] from available experimental data. The simulation is carried out on only half of the geometry owing to symmetry conditions, so slip conditions are imposed on the axis. Static pressure is imposed at the outlet. The profiles are made dimensionless using the half-height of the pipe and the velocity on the axis. Profiles of the first component of velocity and the turbulent kinetic energy are shown at three sections (inlet, middle of pipe, outlet) in Figures 14 and 15, respectively.

Among the three sections the $\tilde{u}_1$-component profiles are similar, which is consistent with the fully developed turbulence hypothesis. However, there are small discrepancies in the level of $\tilde{k}$ between the inlet section and the other two sections. These are due to a small difference in the friction velocity of the wall, $\tilde{k}$ being proportional to the square of the friction velocity. The pressure was made

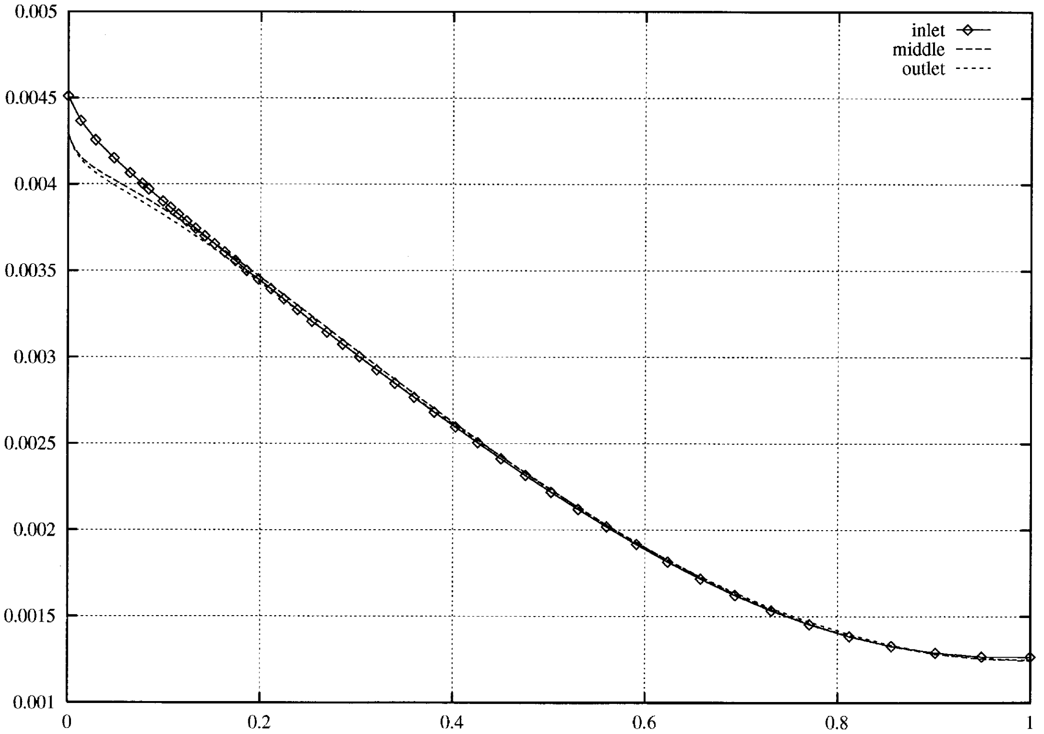

Figure 15. Pipe: profiles of turbulent kinetic energy at inlet, middle and outlet sections

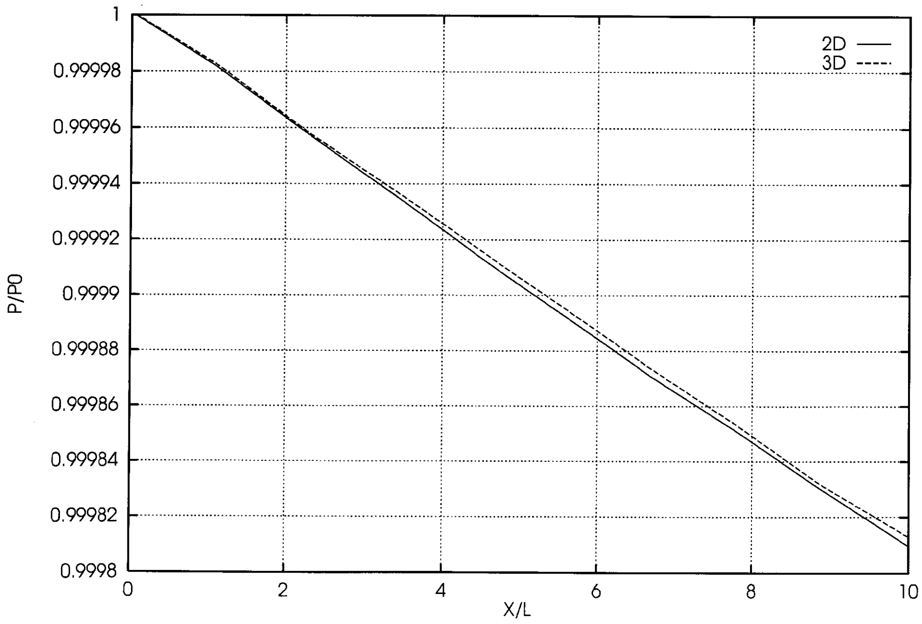

Figure 16. Pipe: static pressure along x-axis

dimensionless using the inlet pressure and is compared with the two-dimensional result. As shown in Figure 16, it is a linear function of x, which is in good agreement with the theory. These results prove the good behaviour of the wall functions for three-dimensional applications.

5. CONCLUSIONS

A three-dimensional method to solve turbulent compressible flows has been presented. The turbulence is described by a standard k–ε model. This numerical method is an extension of a finite volume–finite element method developed to solve the laminar Navier–Stokes equations. Three validation test cases are presented: a low-Mach-number turbulent jet, a compressible shear layer and a three-dimensional pipe. The main characteristics of the flow are well predicted and the converged solutions are obtained much more quickly than with an explicit time integration scheme. The use of k–ε model is very promising and allows this numerical technique to be employed to predict turbulent compressible flows in complex three-dimensional geometries. Industrial applications of this code are under development for predicting flow in the combustion chamber of a gas turbine engine. The work under development includes the improvement of the k–ε model in order to take into account compressibility effects and the introduction of multiple species and combustion with a decoupled approach.

ACKNOWLEDGEMENTS

The authors acknowledge support from CNRS, METRAFU and SNECMA. Thanks are due to the CCVR (Palaiseau, France) where the turbulent jet and compressible mixing layer computations were done.

REFERENCES

1. Y. Wada and M. S. Liou, 'A flux splitting scheme with high-resolution and robustness for discontinuities', *AIAA Paper 94-0083*, 1994.
2. S. Aubert, L. Hallo, P. Ferrand and M. Buffat, 'Numerical behaviour of unsteady waves', *AIAA J.*, **33**, 888–893 (1995).
3. F. Angrand and A. Dervieux, 'Some explicit triangular finite element schemes for Euler equations', *Int. j. numer. methods fluids*, **4**, 749–764 (1984).
4. A. Dervieux, 'Steady Euler simulations using unstructured meshes', *VKI Lect. Ser. 1884-04*, 1985.
5. B. Stoufflet, J. Perriaux, L. Fezoui and A. Dervieux, 'Numerical simulations of 3D hypersonic Euler flows around space vehicles using adapted finite elements', *AIAA Paper 87-0560*, 1987.
6. P. Rostand, 'Sur une méthode de volumes finis en maillage non structuré pour le calcul d'écoulements visqueux compressibles', *Ph.D. Thesis*, Université Paris VI, 1989.
7. C. Le Ribault, 'Simulation des écoulements turbulents compressibles par une méthode mixte éléments finis–volumes finis', *Ph.D. Thesis*, Ecole Centrale Lyon, 1991.
8. C. Olivier, 'Simulation numérique d'écoulements visqueux compressibles laminaires et turbulents', *Ph.D. Thesis*, Université de Nice Sophia Antipolis, 1991.
9. P. L. Roe, 'Approximate Riemann solvers, parameters vectors, and difference schemes', *J. Comput. Phys.*, **43**, 357–372(1981).
10. B. E. Launder and D. B. Spalding, *Mathematical Models of Turbulence*, Academic, London, 1972.
11. L. Hallo, G. Brun, M. Souchet and J. L. Schultz, 'Development of a finite element code for numerical analysis of reacting flows', *AIAA Paper*, 93–5147, 1993.
12. L. Hallo, G. Brun, M. Souchet and S. Aubert, 'Numerical simulation of viscous flow in transonic combustor', in K. Morgan (ed.), *Finite Elements in Fluids*, Pineridge, Swansea, 1993. pp 498–507
13. B. E. Launder and D. B. Spalding, 'The numerical computation of turbulent flows', *Comput. Methods Appl. Mech. Eng.*, **3**, 269–289 (1974).
14. A. Harten and J. M. Hyman, *J. Comput. Phys.*, **50**, 253–269 (1983).
15. B. van Leer, 'Towards the ultimate conservative difference scheme. I: The quest of monotonicity', *Lect. Notes Phys.*, **18**, 163 (1972).
16. F. Fezoui, 'Résolution des équations d'Euler par un schéma de van Leer en éléments finis', *Rapp. Rech. INRIA 358*, 1985.
17. H. Steve, 'Schémas implicites linéarisés décentrés pour les équations d'Euler', *Ph.D. Thesis*, Universié de Provence, Aix-Marseille, 1988.
18. A. Y. Le Roux, *Thèse*, Université de Rennes, 1974.
19. A. Harten, P. D. Lax and B. van Leer, 'On upstream differencing and Godunov type schemes for hyperbolic conservation laws', *SIAM Rev.*, **25**, 35–67 (1983).
20. W. Sacquepee, 'Etude d'écoulements transsoniques par une méthode d'éléments finis–volumes finis', DEA, Ecole Centrale de Lyon, 1991.
21. B. Larrouturou, 'How to preserve the mass fraction positivity when computing multi-component flows', *J. Comput. Phys.*, **95**, 59–84 (1991).
22. J. Steger and R. F. Warming, 'Flux vector splitting for the inviscid gas dynamic with applications to finite-difference methods', *J. Comput. Phys.*, **40**, 263–293 (1981).
23. L. Cambier, W. Ghazzi, J. P. Veuillot and H. Viviand, 'Une approche par domaines pour le calcul d'écoulements compressibles', *ONERA Note Tech. 143*, Chatillon, 1981.
24. L. Hallo, J. L. Munier, M. Buffat and G. Brun, 'Iterative methods for solving implicit non-structured finite volume discretization of Euler equations', *Int. j. numer. methods fluids*, in press.
25. P. Joly, 'Méthodes de gradients conjugués', *Publ. 84016*, Laboratoire d'Analyse Numérique, Université Paris VI, 1984.
26. F. Shakib, T. J. R. Hughes and Z. Johan, 'A multi-element group preconditioned GMRES algorithm for non symmetric systems arising in finite element analysis', *Comput. Methods Appl. Mech. Eng.*, **75**, 455–456 (1989).
27. Y. Saad and M. H. Shultz, 'GMRES: a generalized minimum residual algorithm for solving non symmetric linear system', *SIAM J. Sci. Stat. Comput.*, **7**, 856 (1986).
28. E. M. Bahraoui, 'Contribution à l'étude d'un jet turbulent axisymétrique en présence de forts gradient de température', *Ph.D. Thesis*, Aix-Marseille II, 1987.
29. G. Brun, 'Development et application d'une méthode d'éléménts finis pour le calcul des écoulements turbulents foretement chauffés, *Ph.D. Thesis*, Ecole Centrale de Lyon, 1988.
30. S. G. Gloevel, J. C. Dutton, H. Krier and J. P. Renie, 'Mean and turbulent velocity measurements of supersonic mixing layers', *Exp. Fluids*, **8**, 263–272 (1990).
31. G. Comte-Bellot, 'Contribution à l'étude de la turbulence de conduite', *Ph.D. Thesis*, Université de Grenoble, 1963.
32. P. Cottin, 'Travail de fin d'études', Ecole Centrale de Lyon, 1989.